

Atmospheric and Oceanic Origins of Tropical Precipitation Variability

JIE HE

Princeton University, and NOAA/Geophysical Fluid Dynamics Laboratory, Princeton, New Jersey

CLARA DESER

National Center for Atmospheric Research,^a Boulder, Colorado

BRIAN J. SODEN

Rosenstiel School of Marine and Atmospheric Science, University of Miami, Miami, Florida

(Manuscript received 1 October 2016, in final form 14 January 2017)

ABSTRACT

The intrinsic atmospheric and ocean-induced tropical precipitation variability is studied using millennial control simulations with various degrees of ocean coupling. A comparison between the coupled simulation and the atmosphere-only simulation with climatological sea surface temperatures (SSTs) shows that a substantial amount of tropical precipitation variability is generated without oceanic influence. This intrinsic atmospheric variability features a red noise spectrum from daily to monthly time scales and a white noise spectrum beyond the monthly time scale. The oceanic impact is inappreciable for submonthly time scales but important at interannual and longer time scales. For time scales longer than a year, it enhances precipitation variability throughout much of the tropical oceans and suppresses it in some subtropical areas, preferentially in the summer hemisphere. The sign of the ocean-induced precipitation variability can be inferred from the local precipitation–SST relationship, which largely reflects the local feedbacks between the two, although nonlocal forcing associated with El Niño–Southern Oscillation also plays a role. The thermodynamic and dynamic nature of the ocean-induced precipitation variability is studied by comparing the fully coupled and slab ocean simulations. For time scales longer than a year, equatorial precipitation variability is almost entirely driven by ocean circulation, except in the Atlantic Ocean. In the rest of the tropics, ocean-induced precipitation variability is dominated by mixed layer thermodynamics. Additional analyses indicate that both dynamic and thermodynamic oceanic processes are important for establishing the leading modes of large-scale tropical precipitation variability. On the other hand, ocean dynamics likely dampens tropical Pacific variability at multidecadal time scales and beyond.

1. Introduction

The great dependence of human society and natural ecosystems on rainfall makes precipitation variability an essential aspect of Earth's climate. Precipitation variability

is particularly important in the tropics, as it not only affects local water supply but also regulates climate remotely through the generation and dispersion of Rossby waves (e.g., Sardeshmukh and Hoskins 1988; Barsugli and Battisti 1998; Schneider et al. 2003). Tropical precipitation variability ranges over many time scales, from short-lived weather systems, such as thunderstorms, to intraseasonal phenomena, such as the Madden–Julian oscillation (MJO), to even longer interannual and decadal variations, including El Niño–Southern Oscillation (ENSO). Understanding the origin of tropical precipitation variability across the entire temporal range is among the fundamental objectives of climate science.

The natural variability of precipitation can be considered, to first order, as a superposition of an internal

Denotes content that is immediately available upon publication as open access.

Supplemental information related to this paper is available at the Journals Online website: <http://dx.doi.org/10.1175/JCLI-D-16-0714.s1>.

^aThe National Center for Atmospheric Research is sponsored by the National Science Foundation.

Corresponding author e-mail: Jie He, jie.he@noaa.gov

DOI: 10.1175/JCLI-D-16-0714.1

© 2017 American Meteorological Society. For information regarding reuse of this content and general copyright information, consult the [AMS Copyright Policy](#) (www.ametsoc.org/PUBSReuseLicenses).

part due to intrinsic atmospheric dynamics and an external part via the interaction of atmosphere with land and ocean. In the tropics, it is well accepted that the ocean plays a crucial role through variations in sea surface temperatures (SSTs). Above-normal SSTs often increase the boundary layer moist static energy and induce anomalous convection. A well-known example is the El Niño event, during which the Pacific warm pool shifts eastward, as do deep convection and heavy rainfall. Owing to the ocean's dynamic control on El Niño-related SST variations, this ocean-induced precipitation variability exhibits predictability beyond the 2–3-week time scale of weather noise.

The ocean's role in generating tropical precipitation variability is reflected in the positive local relationship between precipitation and SST over much of the tropical oceans (Trenberth and Shea 2005). However, certain areas (e.g., the southwestern Indian Ocean and the western Pacific Ocean in summer) feature a negative precipitation–SST relationship (Trenberth and Shea 2005; Wu et al. 2006). In these regions, a large portion of precipitation variability likely results from remote SST forcing or intrinsic atmospheric dynamics (Wang et al. 2005; Wu et al. 2006).

As a nonlinear system, the atmosphere exhibits substantial variability of its own (Lorenz 1963). The chaotic behavior of the atmosphere is often simplified as white noise, with no predictability beyond a few weeks (Hasselmann 1976; Frankignoul and Hasselmann 1977). The importance of the atmospheric intrinsic variability has been long recognized in the midlatitudes, where the atmosphere is commonly treated as a stochastic forcing term in the coupled atmosphere–ocean system (e.g., Frankignoul 1985; Barsugli and Battisti 1998). At low frequencies, the atmospheric variability is amplified by feedbacks from the slowly evolving ocean state. The coupling between the atmosphere and ocean in the midlatitudes is primarily thermodynamic (e.g., Frankignoul and Hasselmann 1977; Barsugli and Battisti 1998; Deser et al. 2003); however, dynamical coupling may also be important in some cases, for example for some aspects of the Pacific decadal oscillation (e.g., Schneider and Miller 2001; Schneider and Cornuelle 2005; Kwon and Deser 2007; Newman et al. 2016) and the Atlantic multidecadal oscillation (e.g., Zhang 2008; Zhang et al. 2016; Delworth et al. 2017), although studies by Clement et al. (2015, 2016) have challenged the latter.

In the tropics, however, precipitation variability due to intrinsic atmospheric dynamics has been far less studied compared to its ocean-induced counterpart. The historical emphasis on the ocean-induced precipitation variability is largely due to its greater predictability, but the extent to which it represents the

total precipitation variability at different time scales has yet to be determined. In addition, there is a lack of consensus on whether ocean dynamics plays a leading role in tropical air–sea interaction. For example, some studies found ocean circulation to be important in driving decadal-scale climate variability in the tropical Pacific (e.g., Jin 2001; Luo and Yamagata 2001), whereas other studies argued for thermodynamic coupling between the atmosphere and the ocean mixed layer (e.g., Clement et al. 2011; Okumura 2013; Zhang et al. 2014).

The Community Earth System Model (CESM) Large Ensemble Project (Kay et al. 2015), which includes millennial control simulations with fully coupled, slab ocean and atmosphere-only configurations, provides an ideal opportunity for addressing these issues. In this study, we will analyze the contribution of the atmosphere and ocean to tropical precipitation variability over a wide range of time scales from daily to multi-decadal. The influence of intrinsic atmospheric processes is assessed from the atmosphere-only simulation forced by a prescribed climatological seasonal cycle of SSTs taken from the fully coupled control simulation. By comparing the atmosphere-only simulation with the fully coupled one, we obtain the “ocean induced” component of precipitation variability. We note that this ocean-induced component can arise from intrinsic ocean variability and ocean–atmosphere coupling; we will mainly discuss their combined effect. The thermodynamic and dynamic nature of the ocean-induced precipitation variability is studied by means of the slab ocean and full-depth ocean coupled simulations.

The rest of the study is organized as follows. Section 2 describes the data and methods. The results are presented in section 3, where we quantify the atmospheric and oceanic contributions to tropical precipitation variability at different time scales. The oceanic contribution is then explained by understanding the nature of local precipitation–SST feedbacks. Finally, we present a brief analysis of the spatial characteristics of the leading modes of atmospheric and ocean-induced precipitation variability. The results are summarized and discussed in section 4, along with implications for the simulation of historical tropical precipitation trends.

2. Data and methods

a. Model simulations

We analyze three long preindustrial control simulations from the CESM (Hurrell et al. 2013): an 1800-yr fully coupled run, a 900-yr slab ocean run, and a 2100-yr atmosphere-only run. These simulations differ in their degree of ocean coupling but are all fully coupled with

land. All three simulations use the Community Atmosphere Model (CAM), version 5, and the Community Land Model, version 4, and are run at approximately 1° resolution for all model components. These simulations were conducted as part of the CESM Large Ensemble Project (Kay et al. 2015).

In the slab ocean run (SlabOcean), CAM5 is coupled to a slab ocean model, the depth of which is taken as the climatological annual mean mixed layer depth from the fully coupled run (Coupled). A fixed “ q flux” term, prescribed as a seasonal-varying climatological sea surface heat flux from the Coupled run, is added to the SST equation following Bitz et al. (2012). This accounts for the effect of ocean dynamics on the SST mean state. The SlabOcean run allows for thermodynamic coupling between the atmosphere and the ocean mixed layer but eliminates any impact from variations in the ocean circulation. We will estimate the impact of dynamic ocean coupling from the difference between the Coupled and the SlabOcean runs.

Because of the lack of dynamical ocean coupling, the tropical SST climatology in the SlabOcean run is slightly warmer than that in the Coupled run in all seasons (Fig. S1 in the supplementary material). As a result, the SlabOcean run has slightly larger precipitation in its climatology than the Coupled run in certain oceanic regions (discussed later), which may affect the comparison of precipitation variability and remains a caveat in the interpretation of our results.

The atmosphere-only run uses the monthly climatological seasonal cycle of SST and sea ice from the Coupled run as its lower boundary condition. We will refer to this simulation as ClimSST. Because of the absence of SST variability beyond the mean seasonal cycle, precipitation variability over ocean primarily results from atmospheric intrinsic dynamics. Strictly speaking, however, it also contains land–atmosphere coupled variability, particularly in monsoon regions, where caution must be taken for interpreting the ClimSST run. Nevertheless, since all the simulations have the same land model, presumably intrinsic land–atmosphere variability will be the same in all of our simulations and will not affect their comparison. The difference between the Coupled run and the ClimSST run captures the ocean-induced component of precipitation variability. Note that this precipitation variability results from internal ocean processes, as well as ocean–atmosphere coupling; our experiments do not allow us to differentiate between the two.

To estimate the impact of the lack of two-way coupling in the atmosphere-only simulations, we conduct a 100-yr uncoupled simulation forced by time-varying monthly mean SSTs taken from years 401–500 of the

Coupled run. This simulation will be referred to as FullSST.

b. Observational datasets

To benchmark the simulated precipitation variability, we analyze pentad (5-day mean) precipitation during 1979–2014 from the Global Precipitation Climatology Project (GPCP; Adler et al. 2003; Huffman et al. 2009). The data are recorded on a $2.5^\circ \times 2.5^\circ$ grid and can be downloaded from the JISAO website (http://research.jisao.washington.edu/data_sets/gpcp/daily/pentad.html). Note that fitting the rain gauge–based observations to a rectangular spatial grid inevitably introduces some spatial and temporal averaging, which affects variability. Therefore, we only present the observed results for the purpose of comparing against the simulations, which are also computed on a rectangular grid.

We also analyze monthly precipitation during 1979–2014 from the CPC Merged Analysis of Precipitation (CMAP; <http://www.esrl.noaa.gov/psd/data/gridded/data.cmap.html>) and monthly surface temperature during 1980–2014 from the Goddard Institute for Space Studies (GISS) surface temperature analysis (<http://www.esrl.noaa.gov/psd/data/gridded/data.gistemp.html>). The spatial resolution is $2.5^\circ \times 2.5^\circ$ for the CMAP precipitation and $2^\circ \times 2^\circ$ for the GISS surface temperature. The GISS surface temperature combines data from the Global Historical Climatology Network, version 3 (meteorological stations), the Extended Reconstructed Sea Surface Temperature, version 4 (ocean areas), and the Scientific Committee on Antarctic Research data (Antarctic stations), as detailed in Hansen et al. (2010).

c. Methods

We first remove the linear trend from all datasets, in order to minimize the impact of climate drift from the simulations and anthropogenic forcing from the observations. The climate drift in the simulations is minimal because the simulations are started from a spun-up ocean state (Kay et al. 2015). Before comparing the simulations with the observations, we interpolate the observed data onto the model grid. When calculating the observed air–sea relationships using the CMAP, which contains missing data, the calculation is done only if at least 70% of the months in a given grid box have data.

We divide the total precipitation variability into several frequency bands of interest, including daily–annual, interannual–decadal, decadal, and multidecadal. Each frequency band is isolated by applying Lanczos filtering in the time domain (Duchon 1979). To estimate the amplitude of precipitation variance for each frequency band, we calculate the standard deviation of the filtered data. We validate this approach by summing up the power

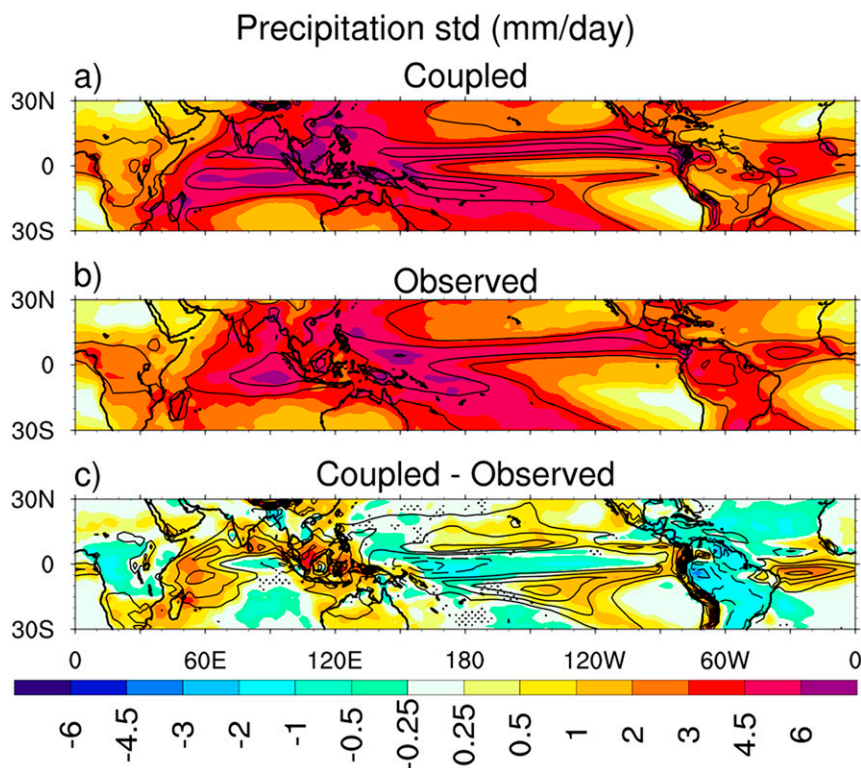


FIG. 1. Mean (contours) and standard deviation (color shading) of pentad precipitation anomalies from (a) the Coupled run, (b) the GPCP, and (c) their difference. Results from the Coupled run are calculated as the average of 50 nonoverlapping 36-yr segments (1800 yr in total), whereas results for the GPCP are calculated using the available 36 yr (1979–2014). Contour interval is 3 mm day^{-1} , starting at 3 mm day^{-1} , in (a) and (b) and 1 mm day^{-1} , starting at 1 mm day^{-1} , in (c). Dashed contours in (c) indicate negative values. Zero contours are omitted. Areas where the difference in variance is not significant at the 99% level based on the F test are stippled in (c). Here and in the rest of the paper, the equivalent sample sizes for statistical tests are determined following (Zwiers and von Storch 1995).

spectra over the specific frequency band, which yields consistent results (figures not shown).

3. Results

a. Overview of precipitation variance across all time scales

It is useful to first examine the total precipitation variance over all time scales resolved by the data. For the pentad GPCP data, we calculate the total variance as the standard deviation of pentad precipitation anomalies during the 36 years (1979–2014) that are available (Fig. 1b). To estimate the total variance from the fully coupled CESM for the same frequency span as the observations, we calculate the standard deviation of pentad precipitation output from each of the 50 nonoverlapping 36-yr segments of the Coupled run and then average across the 50 segments (Fig. 1a).

Both the simulated and observed total precipitation variance fields closely follow the pattern of their

corresponding precipitation climatologies (contours in Figs. 1a,b). For example, regions of large variance correspond to areas with high climatological precipitation, such as the ITCZ, whereas low variance can be found in regions of low mean rainfall, such as the southeastern Pacific. The similarity between patterns of variance and climatology is expected, since precipitation is a positive definite quantity and fluctuates about its mean within the range of zero and its maximum amplitude. There are large biases in the simulated precipitation variance (Fig. 1c). The CESM overestimates the precipitation variance over most of the ITCZ and underestimates it over the equatorial Pacific and the off-equatorial Atlantic Ocean. The pattern of biases in variance is very similar to the pattern of biases in climatology (contour in Fig. 1c).

In Fig. 2, we compare the power spectra of precipitation from GPCP (black lines) and the fully coupled CESM simulation (blue lines) in six tropical regions, which are indicated by the purple boxes in Fig. 2g. In most

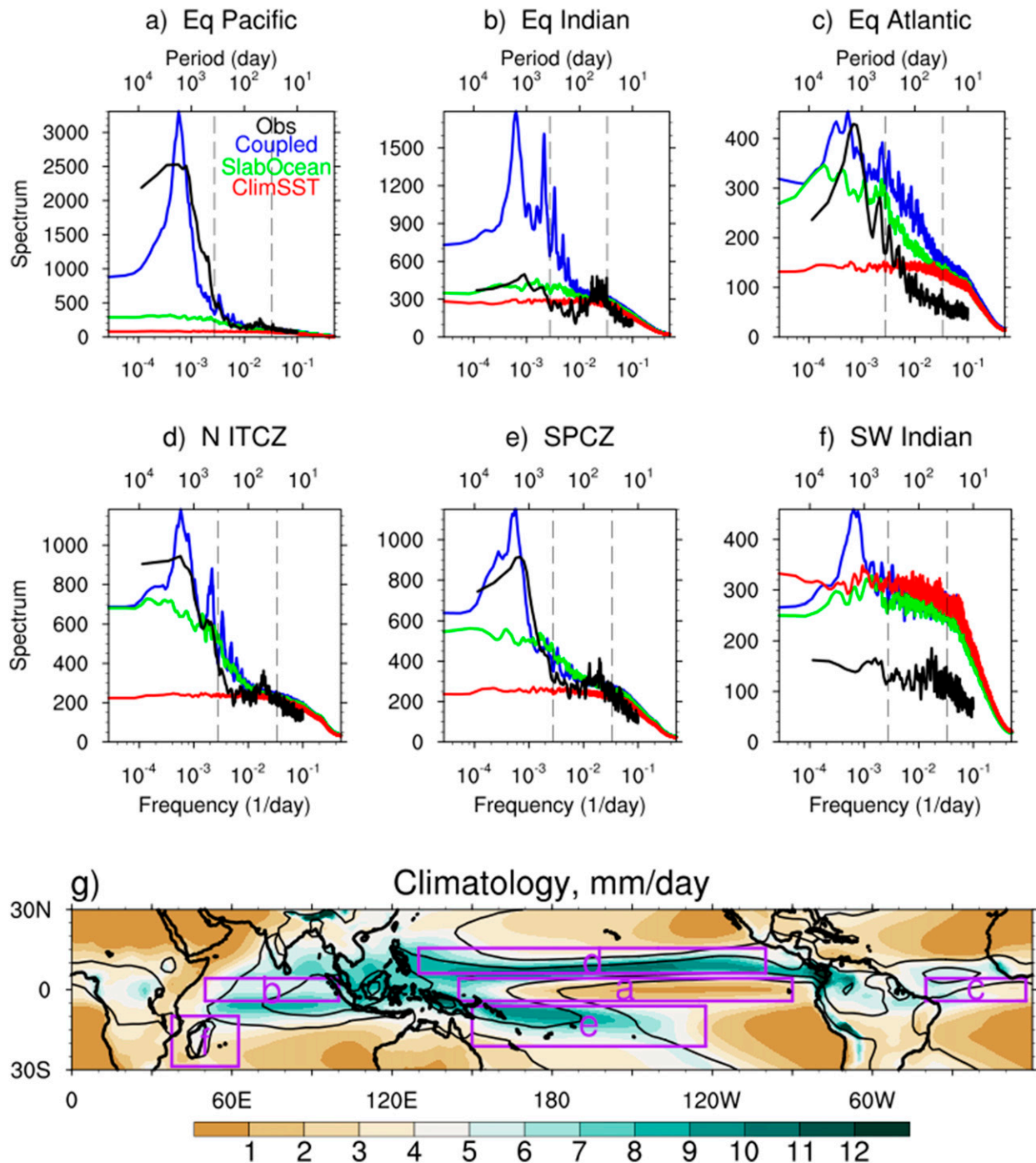


FIG. 2. (a)–(f) Precipitation power spectra averaged over selected regions in the tropics from the GPCP (black) and the Coupled (blue), the SlabOcean (green), and the ClimSST (red) runs. The dashed vertical lines denote the 30-day and 1-yr time scales. (g) The location of the corresponding regions is shown as the purple boxes. The observed spectra are calculated as the average of two partially overlapping 24-yr segments from the 36-yr pentad data. The simulated spectra are calculated as the average of partially overlapping 100-yr segments from the daily output; each segment overlaps the next one by 50 yr. Annual mean precipitation climatology from the Coupled simulation (shading) and the GPCP (contours) in (g). Contour interval is 3 mm day^{-1} , starting at 3 mm day^{-1} .

of these regions (except the equatorial Pacific), the fully coupled CESM overestimates precipitation variance at time scales shorter than 50 days. The general overestimation of high-frequency precipitation variance is consistent with previous findings that most climate models rain too frequently compared to observations, particularly at light rain rates (Pendergrass and Hartmann 2014).

For the three regions in the tropical Pacific (Figs. 2a,d,e), the fully coupled CESM reproduces the observed spectra reasonably well. However, the imprint of an overly vigorous ENSO in the model is evident in most regions, with a spectral peak in the frequency band of approximately $2\text{--}8\text{ yr}^{-1}$ that is narrower and stronger compared to the observations (Fig. 2a). An earlier version of CESM with CAM, version 4, also overestimated the ENSO amplitude (Deser et al. 2012a), which is likely associated with an excessive negative cloud feedback (Tang et al. 2016). For the other three regions outside the Pacific Ocean (Figs. 2b,c,f), the CESM overestimates precipitation variance at almost all frequencies.

Figure 2 also shows the precipitation power spectra from the SlabOcean (green lines) and the ClimSST (red lines) runs. (Note that the ClimSST run is forced with monthly climatological SST and thereby does not include submonthly SST variability; however, a brief analysis in Fig. S2 of the supplementary material indicates that such an experimental setup should not affect the interpretation of our results.) The spectra from the ClimSST run resemble that arising from a red noise process with increasing variance from daily to monthly time scales. Beyond the monthly time scale, the uncoupled spectra are virtually flat, which is consistent with the common assumption that atmospheric intrinsic variability is essentially white noise (e.g., Hasselmann 1976; Frankignoul and Hasselmann 1977). The precipitation variability from the SlabOcean run also features a red noise spectrum. The time scale beyond which the spectra become white varies with region, but it is generally close to or longer than a year. Compared to the ClimSST run, the precipitation variability from the SlabOcean run has similar variance at high frequencies and generally larger variance at low frequencies. This is analogous to the first-order explanation for the generation of climate variability in midlatitudes, where atmospheric intrinsic variability is generally amplified at low frequencies through the influence of more slowly evolving SST anomalies, which in turn are due to the integrated thermodynamic response of the ocean mixed layer to intrinsic atmospheric variability (Hasselmann 1976; Frankignoul and Hasselmann 1977; Frankignoul 1985).

Considering the substantial oceanic impact on precipitation variability beyond the monthly time scale and the close relationship between precipitation variability

and precipitation climatology, it is necessary to examine whether oceanic variability also affects precipitation climatology. As shown in Fig. 3a, there are considerable discrepancies in the long-term mean precipitation between the Coupled and ClimSST runs, despite their virtually identical SST climatologies (Fig. S1). The inclusion of SST variability increases climatological precipitation in the equatorial Pacific by 25%–45% and moderately reduces it by 15% or less in certain off-equatorial regions, including the northeastern and southeastern Pacific, the Maritime Continent and the adjacent oceanic regions, the North Atlantic, and the southwestern Indian Ocean. The increase at the equatorial Pacific is most likely due to the nonlinear rectification effect of SST forcing (i.e., positive SST anomalies can increase precipitation substantially, whereas negative SST anomalies only have a minor effect since the mean precipitation is low to begin with). There are also noticeable discrepancies over land, where SST variability generally increases precipitation climatology north of the equator and reduces it south of the equator. As we shall see, the sign of the oceanic contribution to precipitation climatology is generally consistent with that to precipitation variance.

The climatological precipitation discrepancies in the ClimSST run can be attributed to either the lack of SST variability or the lack of two-way coupling; the latter eliminates any SST response to atmospheric forcing and could degrade the simulation of tropical climate (e.g., Wang et al. 2005; Wu et al. 2006). In Fig. 3b, we compare the Coupled run with the FullSST run, in which the monthly varying SSTs from a 100-yr segment of the Coupled run are prescribed. The FullSST run does not substantially underestimate precipitation climatology from the Coupled run in the equatorial Pacific but still shows generally similar discrepancies as those in the ClimSST run over the rest of the tropics, indicating that the lack of two-way coupling could cause the differences between ClimSST and Coupled runs outside of the equatorial Pacific. This is in conflict with previous studies, which suggested that two-way coupling is not necessary in simulating the time-averaged climate (Skinner et al. 2012; He and Soden 2016). Note, however, that the FullSST run is only 100 years long and therefore might not provide a robust estimation of precipitation climatology (note that the differences between Coupled and FullSST runs are generally less than 15% over the tropical ocean and not statistically significant).

Discrepancies in precipitation climatology can also be found between the Coupled and SlabOcean runs (Fig. 3c). This may be partially due to the SST biases (Fig. S1). However, in the equatorial Pacific, precipitation climatology is 15%–35% larger in the Coupled run despite the

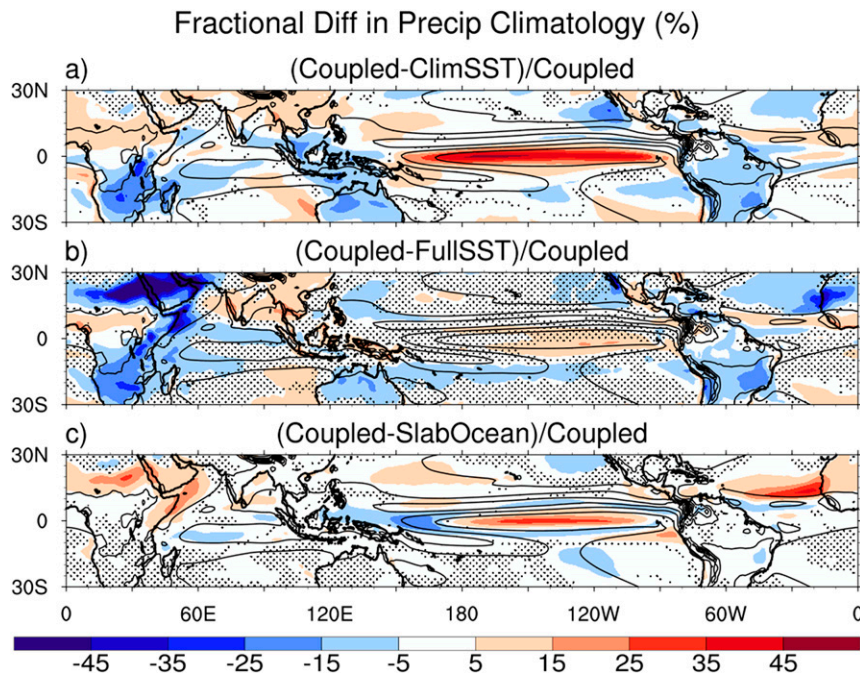


FIG. 3. Fractional difference in annual mean precipitation climatology (color shading) between (a) Coupled and ClimSST runs, (b) Coupled and FullSST runs, and (c) Coupled and SlabOcean runs. The fractional difference is shown as a percentage relative to the Coupled climatology. Annual mean precipitation climatology from the Coupled run is plotted as contours. Contour interval is 3 mm day^{-1} , starting at 3 mm day^{-1} . Areas where the difference in variance is not significant at the 99% level based on the Student's t test are stippled. There is much more stippling in (b) than in (a) and (c), mainly because of the relatively small sample size of the FullSST run.

lower SST, which suggests that coupling with ocean dynamics increases precipitation climatology. In addition, the Coupled run shows larger precipitation climatology than the SlabOcean run in the north equatorial Atlantic (by 5%–45%) and parts of northern Africa (by 5%–25%).

b. Precipitation variance at daily to yearly time scales

The regional average precipitation spectra in Fig. 2 suggest that the relative role of ocean in driving precipitation variability varies with time scale. In Fig. 4, we present precipitation variance from the Coupled and ClimSST runs at subannual and beyond-annual time scales. Since the uncoupled precipitation variance is distributed according to an approximately red noise process in the frequency domain (Fig. 2), its spatial pattern at individual frequency bands is also similar to the pattern of precipitation climatology (Figs. 4b,f).

For the subannual time scale, the ocean-induced precipitation variability (i.e., Coupled – ClimSST runs) is small (Fig. 4c) and consists of less than 30% of the total variance in almost the entire tropics, except at the central equatorial Pacific (Fig. 4d). Particularly at the sub-monthly time scale, precipitation variance is very similar

between the Coupled and ClimSST runs (Fig. 2). The insignificance of ocean at submonthly time scales is largely due to the lack of substantial SST variability on these time scales (Fig. S3 in the supplementary material). However, this result might be susceptible to the model's inadequate simulation of phenomena, such as the MJO, which might be better represented with improved parameterization and higher resolution (Boyle et al. 2015).

As shown in the right column of Fig. 4, the relative impact of ocean is larger at lower frequencies. For time scales longer than a year, ocean amplifies precipitation variability over most of the tropical oceans. Particularly within 10° of the equator, oceanic variability generally contributes to more than 30% of the total precipitation variance (Fig. 4h). In the equatorial Pacific, precipitation variability is almost entirely driven by ocean (values $>80\%$). In contrast to the ClimSST run (Fig. 4f), precipitation variance in the Coupled run (Fig. 4e) has its maximum values on the equatorward sides of the climatology maxima (ITCZ and SPCZ) in the Pacific at this frequency band. In certain regions (e.g., the southwestern Indian Ocean, the Bay of Bengal, and the northeastern Pacific), however, ocean suppresses

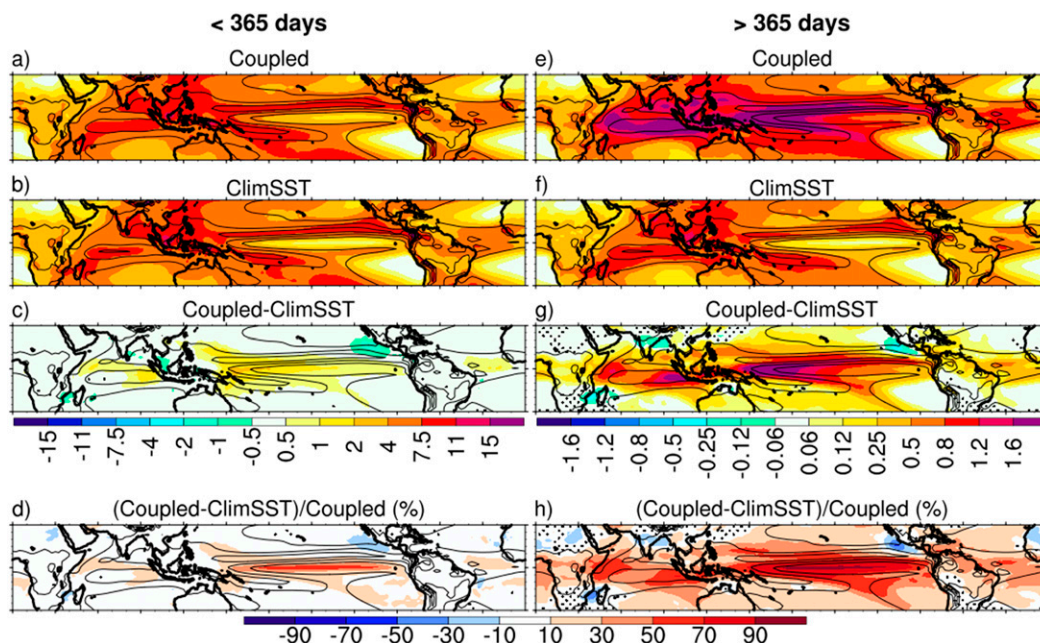


FIG. 4. Precipitation standard deviation (mm day^{-1} ; color shading) from the (a),(e) Coupled run; (b),(f) ClimSST run; and (c),(g) their difference and (d),(h) their fractional difference, using (left) 365-day high-pass and (right) 365-day low-pass daily precipitation anomalies. Contours show the annual mean precipitation climatology from the Coupled run in (a),(e),(c),(g),(d),(h) and from the ClimSST run in (b) and (f). Contour interval is 3 mm day^{-1} , starting at 3 mm day^{-1} . Note that different scales are used to plot the results for the two time scales. The scales of the color bars are chosen in a way that the uncoupled precipitation variance [(b) and (f)] appears similarly for the two time scales. Areas where the difference in variance is not significant at the 99% level based on the F test are stippled in (c),(g),(d),(h). The lack of stippling in (c) and (d) is mainly due to the large sample size.

precipitation variability (Figs. 4g,h). The oceanic contribution to low-frequency precipitation variability as well as its seasonality will be further discussed in the next two sections.

c. Precipitation variance at interannual and longer time scales

In this section, we present tropical precipitation variability on interannual and longer time scales ($>2 \text{ yr}$). Subdividing this frequency band into three frequency bands (2–10, 10–50, and $>50 \text{ yr}$) does not provide additional insight, as their characteristics are very similar to those based on $>2 \text{ yr}$ for the analyses presented here (Figs. S4 and S5 in the supplementary material). In this and the following sections, we analyze each season separately. Results will be presented for December–February (DJF) and June–August (JJA); results for March–May and September–November are similar to those for DJF and JJA, respectively, and will not be presented here.

The patterns of precipitation variance on interannual and longer time scales in the ClimSST run are again similar to their climatologies, both in DJF and JJA (not shown). Here, we focus on the role of ocean by comparing the fractional difference in precipitation variance

among the three model configurations. Ocean enhances precipitation variability over most tropical ocean regions, particularly at the equatorial Pacific, where it generates over 90% of the total variability in DJF and over 70% in JJA (Figs. 5a and 6a, respectively). On the other hand, ocean suppresses precipitation variability in certain off-equatorial oceanic regions. For DJF (Fig. 5a), these regions include the southwestern Indian Ocean, the center of the South Pacific convergence zone (SPCZ) and the subtropical central North Pacific (the latter only for the decadal time scale and beyond; Fig. S4). For JJA (Fig. 6a), these regions include the northeastern Pacific, the South China Sea, and the Bay of Bengal. Interestingly, the negative oceanic contribution primarily occurs in the summer hemisphere. We will further analyze the pattern of the ocean-induced precipitation variance in the next section. The magnitude of the positive oceanic contribution peaks at the interannual time scale in the equatorial Pacific and the equatorial Indian Ocean, consistent with Fig. 2. The impact of the ocean also extends to land regions. In particular, it induces positive precipitation variance in North and central Africa in DJF (Fig. 5a) and in South America in JJA (Fig. 6a).

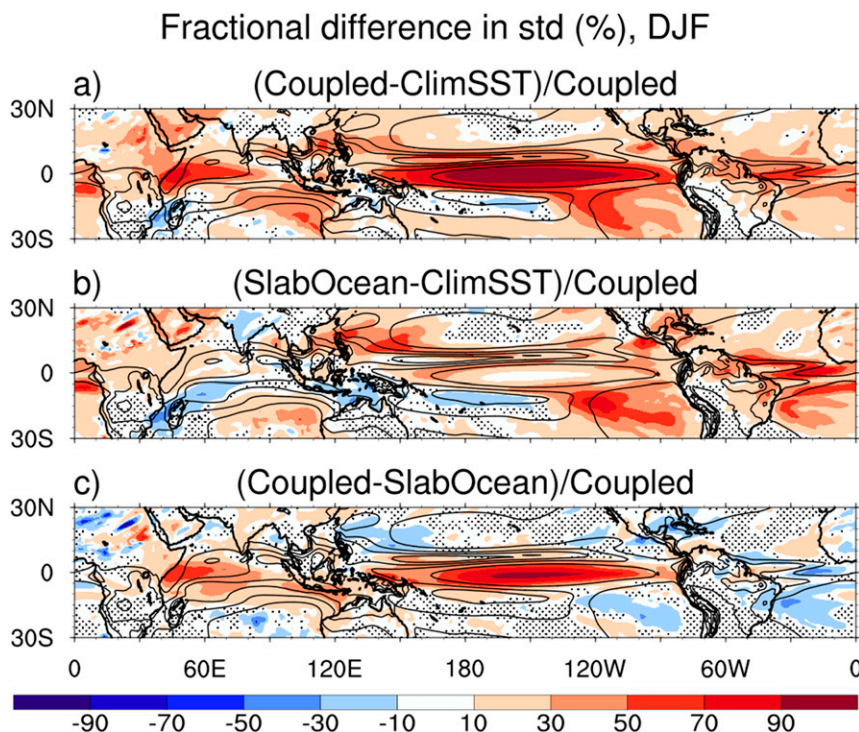


FIG. 5. Fractional difference in precipitation standard deviation (color shading) between (a) Coupled and ClimSST, (b) SlabOcean and ClimSST, and (c) Coupled and SlabOcean using yearly DJF precipitation anomalies. The fractional difference is shown as a percentage relative to the Coupled standard deviation. DJF mean precipitation climatology from the Coupled run is plotted as contours. Contour interval is 3 mm day^{-1} , starting at 3 mm day^{-1} . Areas where the difference in variance is not significant at the 99% level based on the F test are stippled.

In the off-equatorial regions, both the positive and negative ocean-induced precipitation variability are largely reproduced by the SlabOcean run and are therefore primarily associated with mixed layer thermodynamic processes (Figs. 5b and 6b). At the equator, however, most of the precipitation variability requires coupling with ocean dynamics (Figs. 5c and 6c). The DJF equatorial Atlantic is an exception where mixed layer thermodynamics dominate. In addition, the Coupled run generally simulates less precipitation variability in the off-equatorial regions than the SlabOcean run, which likely suggests a negative contribution from ocean circulation but could also be caused by the lower climatological SST in the Coupled run (Fig. S1).

d. Local air–sea relationships

The pattern of the ocean-induced precipitation variability shown in Figs. 7a and 8a suggests positive and negative feedbacks between precipitation and SST anomalies. If we assume that these feedbacks are primarily local and instantaneous for the time scales considered here (i.e., precipitation and SST adjust to each other's variations well within a year), we should be able to

understand them through the simultaneous, pointwise correlation between precipitation and SST. Of course, local correlations may also reflect nonlocal controls on precipitation and SST (e.g., those due to atmospheric and oceanic teleconnections). These will also be taken into account in our discussion below.

Figures 7b and 8b show the local pointwise regression coefficients between precipitation and surface temperature anomalies in DJF and JJA, respectively, from the Coupled run ($\text{mm day}^{-1} \text{K}^{-1}$). Note that no time filtering has been applied, other than the use of seasonal means. In both DJF and JJA, the precipitation–SST regression is positive over most of the tropical oceans, with values exceeding $2.5 \text{ mm day}^{-1} \text{K}^{-1}$ over the western equatorial Pacific and the equatorial Indian Ocean. On the other hand, the regression is negative in the center of the ITCZ and SPCZ, as well as some areas of the subtropical oceans (e.g., the southwestern Indian Ocean in DJF and the Bay of Bengal and the South China Sea in JJA) and many land regions, particularly in the summer hemisphere.

Previous studies (Trenberth and Shea 2005; Wang et al. 2005; Wu et al. 2006) showed that the local precipitation–SST relationship characterizes the basic nature of

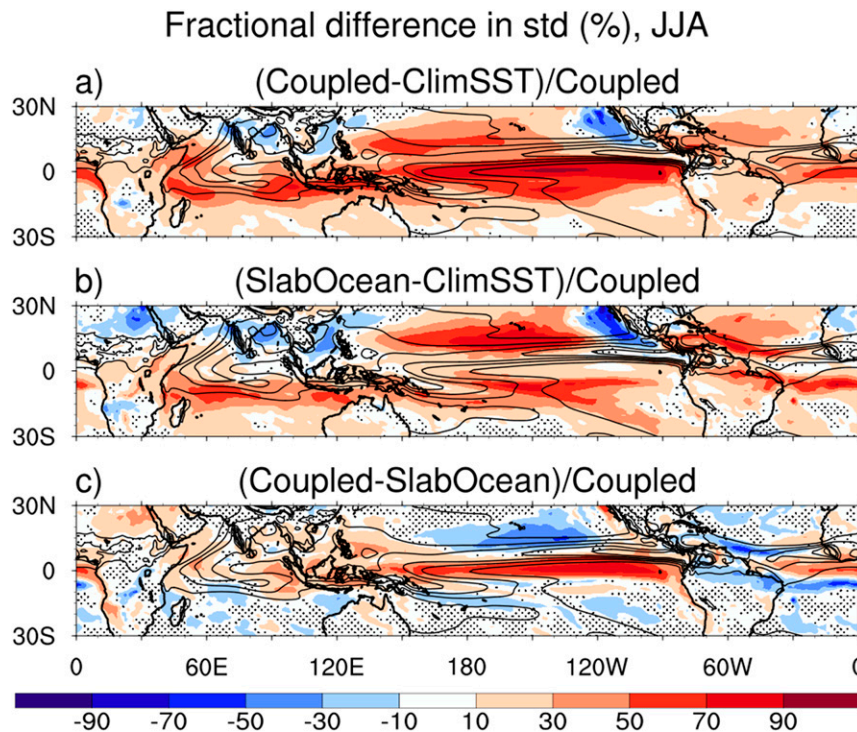


FIG. 6. As in Fig. 5, but for JJA.

precipitation–SST interaction. In the absence of remote SST forcing (such as that associated with ENSO, which will be discussed later), the relationship is positive when SST forces precipitation and negative when precipitation forces SST. A negative relationship in the absence of nonlocal effects is primarily associated with cloud radiative cooling and cold air downdrafts associated with convection (e.g., Waliser and Graham 1993; Sud et al. 1999). In the absence of precipitation-forcing SST, precipitation generally increases with increasing local SST, and vice versa. We can determine this from the atmosphere-only simulations with prescribed SST anomalies, in which a positive precipitation–SST relationship is found throughout the tropical oceans (Wang et al. 2005; Wu et al. 2006). In a coupled system, however, the relationship can be negative. In this case, a positive precipitation anomaly can cause a local cooling of SST, which will act to reduce precipitation and suppress the initial precipitation anomaly.

Therefore, we can expect ocean to locally amplify precipitation variability where SST forcing dominates (i.e., positive precipitation–SST regression) and locally suppress precipitation variability where precipitation forcing dominates (i.e., negative precipitation–SST regression). Indeed, the pattern of the precipitation–SST regression value over ocean (Figs. 7b and 8b) is very similar to that of the oceanic contribution to precipitation

variance (i.e., Coupled vs ClimSST; Figs. 8a and 9a). In general, ocean amplifies precipitation variability in regions of positive precipitation–SST regression, and vice versa. However, there are exceptions in certain parts of the ITCZ (i.e., the northern ITCZ in DJF and both the northern and southern ITCZ in JJA), where ocean amplifies precipitation variability despite a negative precipitation–SST regression. A common characteristic of these regions is the presence of large horizontal SST gradients. It is likely that most of the local precipitation variability is driven by variations in the SST gradient rather than the amplitude of the SST itself (Lindzen and Nigam 1987; Back and Bretherton 2009; Li and Carbone 2012). Indeed, in the northern ITCZ region in DJF, we find a moderate negative correlation between precipitation and the local Laplacian of SST (Fig. S6 in the supplementary material). On the other hand, such negative precipitation–SST regressions can also result from remote SST forcing and, in that case, may not serve as an indicator of negative ocean-induced precipitation variability, as we shall show next.

Previous studies suggested that ENSO-related SST anomalies may be particularly effective in modulating the precipitation–SST relationship through its ability to shift precipitation at large scales (Trenberth and Shea 2005; Wu et al. 2006). In Figs. 9 and 10, we calculate the precipitation–SST regression for ENSO years

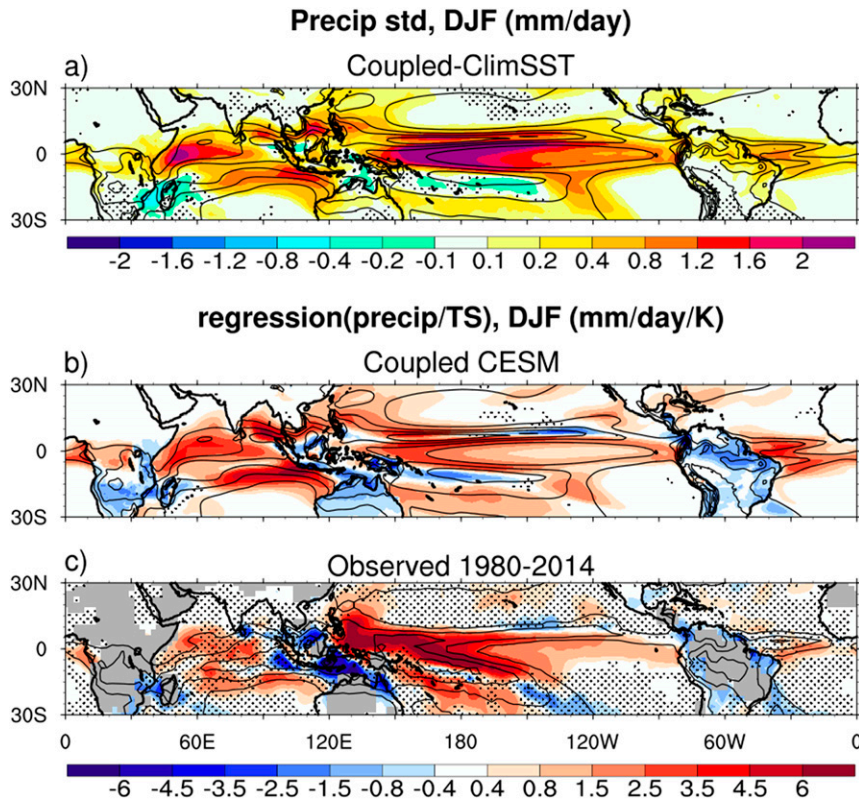


FIG. 7. (a) Difference in precipitation standard deviation between the Coupled and SlabOcean runs using yearly DJF mean precipitation, and linear regressions of precipitation anomaly onto surface temperature anomaly using yearly DJF output (b) from the Coupled run and (c) from CMAP and GISS surface temperature analysis. Regions where more than 30% of the data are missing are filled in gray. Contours are the DJF precipitation climatology from the Coupled run in (a) and (b) and the observed DJF precipitation climatology in (c). Contour interval is 3 mm day^{-1} , starting from 3 mm day^{-1} . Stippling in (a) indicates that the difference in variance is not significant at the 99% level based on the F test, whereas stippling in (b) and (c) indicates that the linear correlation between precipitation and surface temperature is not significant at the 99% level based on the two-sided Student's t test.

(Figs. 9a and 10a) and non-ENSO years (Figs. 9b and 10b) separately. The difference between the two (Figs. 9c and 10c) provides an estimation of the impact of ENSO. The ENSO-induced precipitation–SST regression (Figs. 9c and 10c) has about the same magnitude as the total precipitation–SST regression (Figs. 7b and 8b). The pattern of the ENSO-induced precipitation–SST regression (Figs. 9c and 10c) is essentially determined by whether the local SST and precipitation anomalies have the same sign during ENSO (Fig. S8 in the supplementary material). In the equatorial Pacific and the eastern Indian Ocean, where precipitation increases during El Niño and decreases during La Niña, ENSO drives a positive precipitation–SST regression. The positive regression suggests that the SSTs could be more likely to cross the convection threshold during ENSO, causing an enhanced precipitation response to the SST anomaly. In the off-equatorial Pacific and the western Indian Ocean, ENSO

drives a negative precipitation–SST regression. These regions experience a lack of rainfall because of the drastic equatorial shift of convection during El Niño, despite the positive local SST anomaly. The clear-sky condition may in turn enhance the warming of the SST (Klein et al. 1999; Shinoda et al. 2004; Chiang and Lintner 2005). Interestingly, the remote influence of equatorial Pacific SST anomalies is only effective at the interannual time scale and virtually nonexistent at the decadal time scale and beyond (latter not shown).

Figures 9d and 10d show the difference in precipitation variance between ENSO years and non-ENSO years. The ENSO-induced precipitation variability is positive over most of the tropics and is most appreciable over regions where ENSO substantially affects the precipitation–SST regression (Figs. 9c and 10c). Note that, even in regions where ENSO induces a negative precipitation–SST regression, precipitation variability is

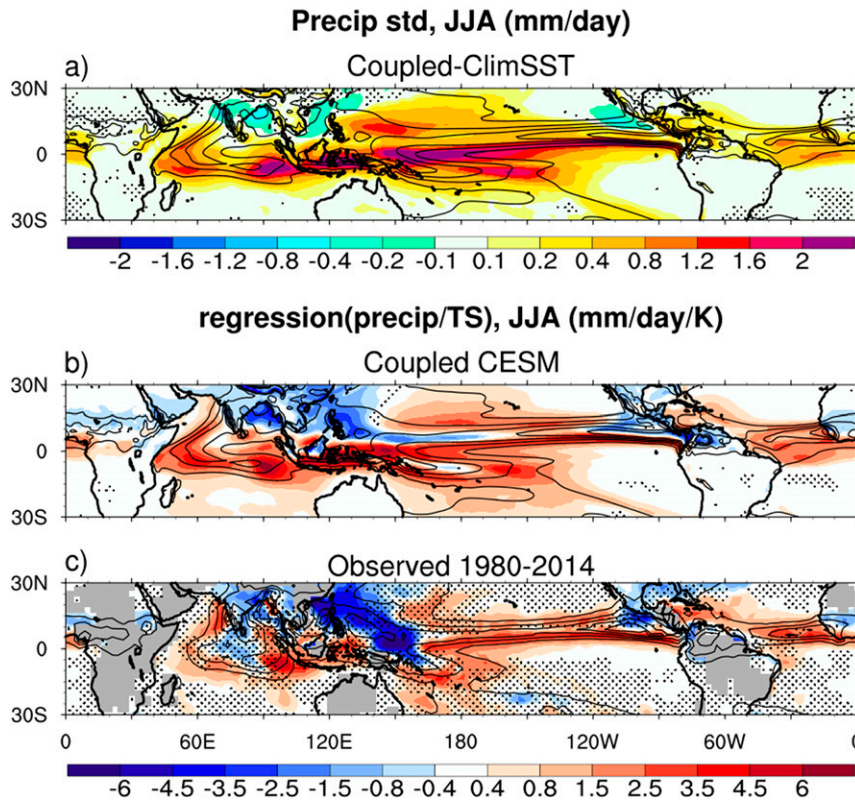


FIG. 8. As in Fig. 7, but for JJA.

still generally enhanced by ENSO. Such enhanced variability is most likely a result of remote SST forcing, since the ENSO-induced local precipitation–SST feedbacks act to suppress precipitation variability.

To benchmark the CEM simulated precipitation–SST regression, we present the observed precipitation–SST regression in Figs. 7c and 8c. Because of the relatively short record of the observations, most of the tropics do not show statistically significant correlations (stippling in Figs. 7c and 8c). Nevertheless, the model is able to reproduce the basic structure of the observed precipitation–SST regression, and most of the discrepancies between the two are related to biases in the model’s mean state. For example, the tendency for negative regression values within the centers of the precipitation maxima (SPCZ, ITCZ, and the Maritime Continent) is present to some degree in observations, although the exact geographical locations may not coincide with those simulated as a result of the biased mean state in the model. On the other hand, some of the discrepancies appear unrelated to the climatological biases and are likely a result of the misrepresentation of the precipitation–SST feedbacks. For example, in DJF, the CEM underestimates the negative regression in the Maritime Continent and the adjacent oceanic regions and the positive regression in the western

equatorial Pacific; it also overestimates the positive regression in the equatorial Atlantic. In JJA, the negative regression in the summer Asian monsoon regions is generally stronger and extends farther south in the observations.

e. Spatial modes of precipitation variability

The substantial precipitation variability simulated in the SlabOcean and ClimSST runs merits more detailed analyses on its spatial and temporal characteristics. To that end, we performed and compared EOF analyses in various tropical regions at interannual (<10 yr), decadal (10–50 yr), and multidecadal (>50 yr) time scales. We only present results based on EOFs over the tropical Pacific, a region that has historically attracted great attention.

Figures 11 and 12 show global maps of annual mean precipitation and sea level pressure (SLP) anomalies correlated with the first principal component (PC) of precipitation anomalies within the tropical Pacific region (outlined by the red rectangle) for each time scale. The Coupled (Figs. 11a–c), SlabOcean (Figs. 11d–f), and ClimSST (Fig. 12) runs all simulate spatially coherent precipitation and circulation patterns within the tropical Pacific at all time scales. Unlike the Coupled run, which shows a decrease in explained variance with increasing

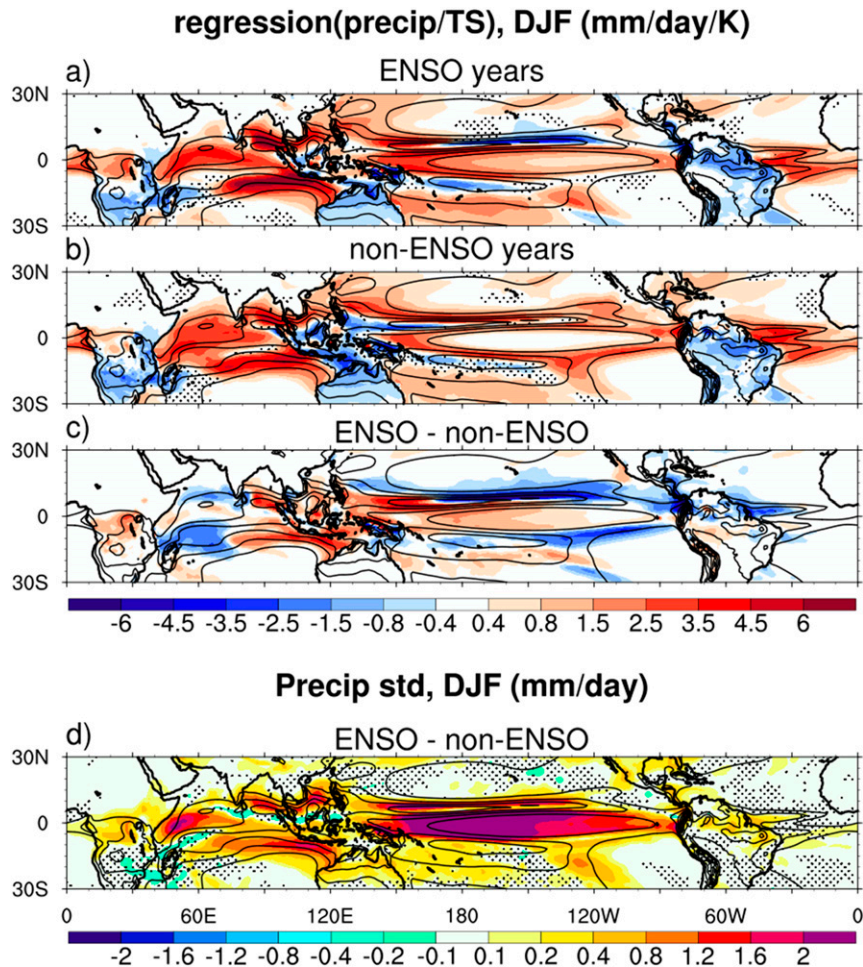


FIG. 9. Linear regression of precipitation anomaly onto surface temperature anomaly (color shading) using yearly DJF output from the Coupled run for (a) ENSO years, during which the yearly DJF SST anomaly in the Niño-3.4 region exceeds one standard deviation, (b) non-ENSO years, during which the SST anomaly of Niño-3.4 is less than 30% standard deviation, and (c) their difference. (d) Difference in the standard deviation of yearly DJF precipitation between the ENSO years and non-ENSO years in the Coupled run. DJF precipitation climatology from the Coupled run is plotted as contours. Contour interval is 3 mm day^{-1} . Stippling in (a),(b),(d) indicates the results of the statistical tests and is plotted the same as in Fig. 7.

time scale, the SlabOcean run shows an increase, and the ClimSST run shows almost no change. Indeed, the variance explained in the Coupled run diminishes by nearly a factor of 2 (from 38.4% to 23.1%), whereas that in the SlabOcean run more than doubles (from 13.9% to 29.3%) between interannual and multidecadal time scales. The variance explained in the ClimSST run is much smaller than that in the other two runs at all time scales (6%–7%).

For all three time scales, the first EOF of the Coupled run exhibits an ENSO-like precipitation pattern in the tropical Pacific with teleconnections extending to nearly the entire globe. Particularly at the interannual time scale, the spatial coherence of the global precipitation and SLP patterns associated with the first EOF in the

Coupled run (Fig. 11a) is unmatched by that from the SlabOcean (Fig. 11d) and ClimSST (Fig. 12a) runs. The first EOF of the SlabOcean run features a similar ENSO-like pattern at the multidecadal time scale, although the remote teleconnections differ (Fig. 11f). However, at the interannual (Fig. 11d) and decadal (Fig. 11e) time scale, the leading mode of variability shows a distinctive structure with an out-of-phase relationship between the equatorial Pacific and the northern subtropics. For these two time scales, the ENSO-like mode appears as the second EOF in the SlabOcean run (Fig. S9 in the supplementary material). Although the ENSO-like mode in the SlabOcean run is generally similar to that in the Coupled run, it shows an embedded negative precipitation

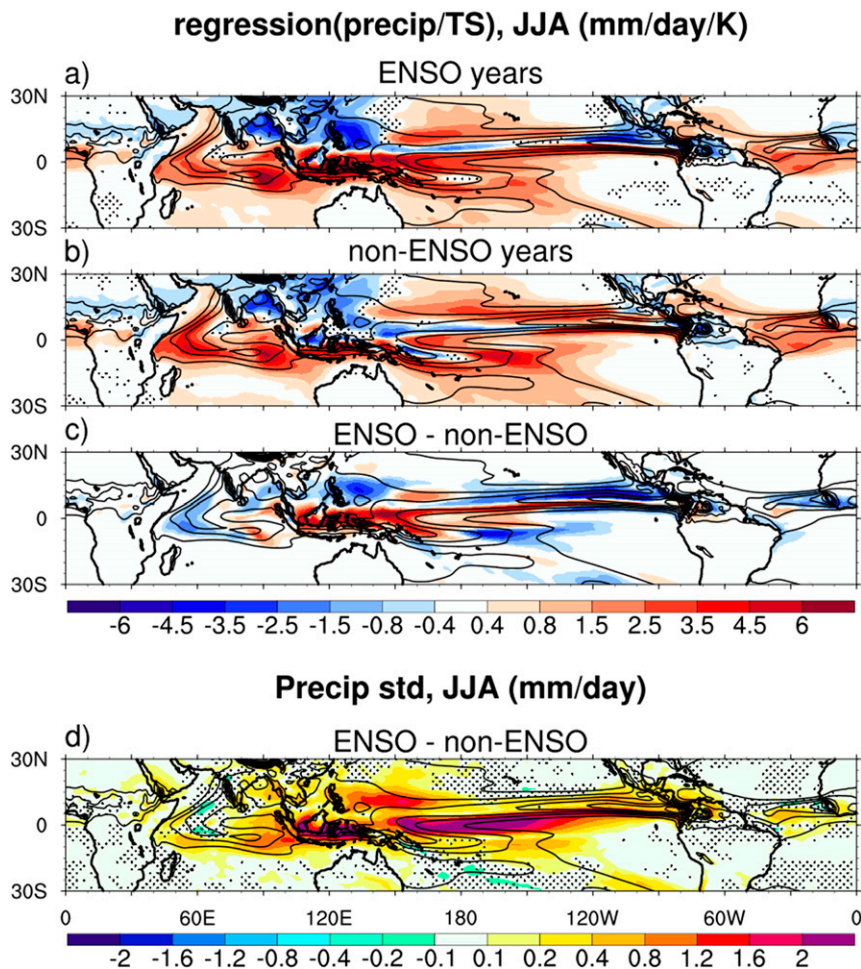


FIG. 10. As in Fig. 9, but for JJA.

anomaly right at the equator, which is absent in the Coupled run. This difference can be found for all three time scales and likely reflects the strong dependence of precipitation variability on coupling with ocean dynamics at the equatorial Pacific (Figs. 5c and 6c).

The first mode of the ClimSST run features a zonally banded pattern in the tropical Pacific and explains a relatively small portion of the total precipitation variance (Fig. 12). This pattern differs substantially from the ENSO-like pattern because of the lack of ocean coupling. Compared to the Coupled and SlabOcean runs, the ClimSST run has the most temporally consistent EOF modes, with similar patterns and amplitude across all time scales. This is in agreement with the previous conclusion that the uncoupled tropical precipitation variability is essentially a white noise beyond the monthly time scale.

An interesting feature of Fig. 11 is the pronounced extratropical circulation patterns associated with the tropical Pacific precipitation variability, which occur in

the Coupled run at all time scales and in the SlabOcean run mainly at the multidecadal time scale. For example, most of these show a negative SLP anomaly in the North Pacific and a positive SLP anomaly in the southeastern Pacific, as well as connections to the Southern Ocean and Atlantic basin of varying strength. It is well known that tropical precipitation anomalies can modulate extratropical circulation via the generation and dispersion of Rossby waves (e.g., Sardeshmukh and Hoskins 1988; Barsugli and Battisti 1998; Schneider et al. 2003). On the other hand, the extratropical circulation can also energize tropical climate variability. It has been shown that the atmospheric stochastic forcing from both the North Pacific (e.g., Pierce et al. 2000; Di Lorenzo et al. 2015) and the South Pacific (e.g., Okumura 2013; Zhang et al. 2014) are particularly important for the development of the ENSO-like pattern of variability. A question that often appears in these studies is how ocean coupling facilitates these tropical–extratropical teleconnections. Here, we present a brief analysis on this question.

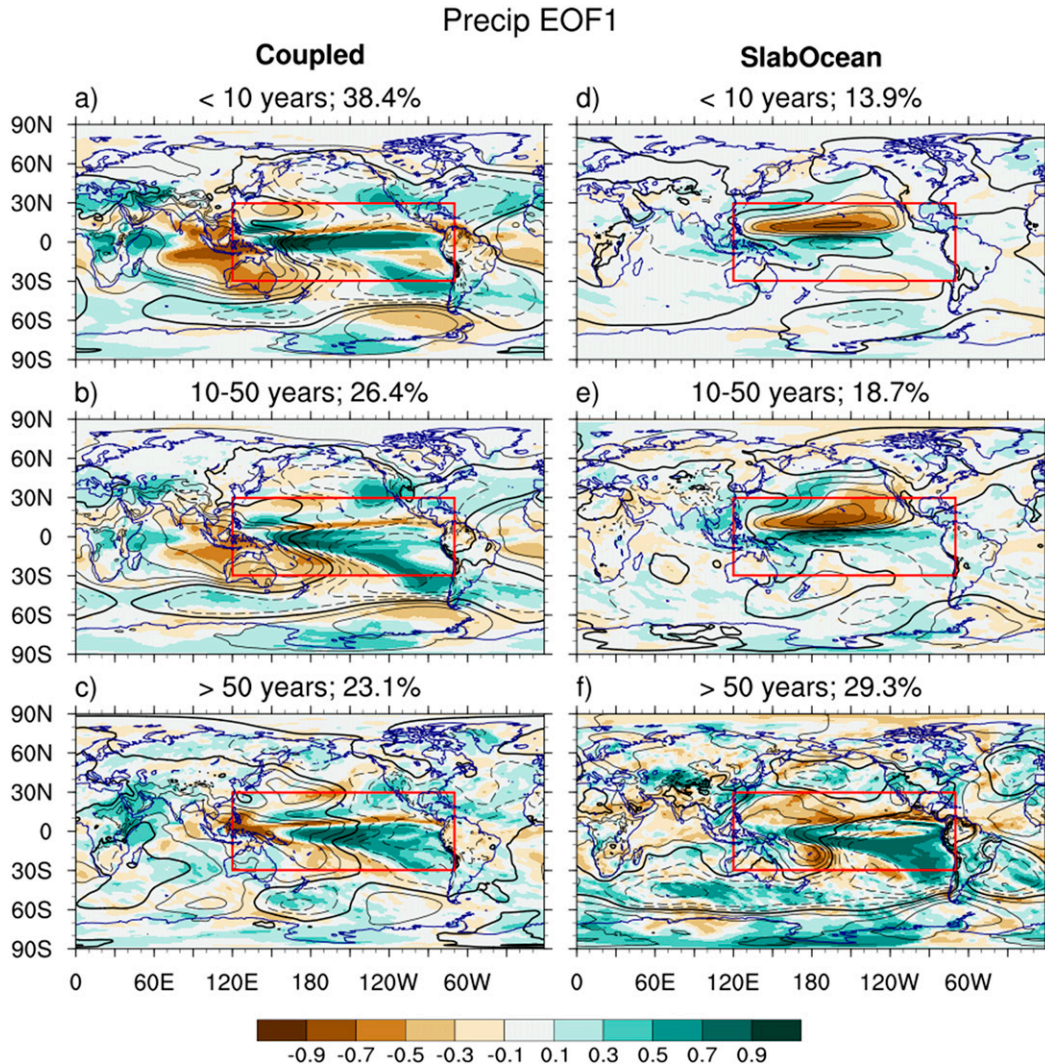


FIG. 11. Linear correlation of precipitation (shading) and SLP (contour) anomalies with the leading PC of precipitation anomalies in the Indo-Pacific region, which is marked by the red boxes. Data are the annual mean output filtered by (a),(d) 10-yr high pass, (b),(e) 10-50-yr bandpass, and (c),(f) 50-yr low pass. Results are from the (left) Coupled and (right) SlabOcean runs. Contour interval is 0.2. Dashed contours represent negative values. The zero contour is thickened. Variance explained by EOF1 is shown in the title of each panel.

In Fig. 13, we show global maps of annual mean precipitation and SLP correlations with the leading mode of SLP variability in the extratropical South Pacific (15° – 70° S, 170° E– 70° W; outlined by the red box) at each time scale. The region chosen for the EOF analysis is defined in the same way as by Okumura (2013), who investigated the decadal tropical–extratropical teleconnections in a similar way using the Community Climate System Model, version 4. Both the Coupled and SlabOcean runs show a local Pacific–South American pattern (PSA; with a low pressure anomaly off the coast of Chile and an adjacent high pressure anomaly to its south) embedded within a larger southern annular mode structure at all

three time scales, consistent with Okumura (2013). For all time scales in the Coupled run and the SlabOcean run, the PSA is associated with a meridional dipole pattern of precipitation in the South Pacific; however, the tropical precipitation anomalies are not consistent. The ClimSST run also simulates a PSA mode, indicating that such a mode can be generated through atmospheric intrinsic dynamics. However, its correlation with tropical precipitation is negligible (figures not shown).

A key distinction between the two coupled model configurations is that the connection to the tropical Pacific (both precipitation and SLP) strengthens as the time scale lengthens in the case of the SlabOcean run

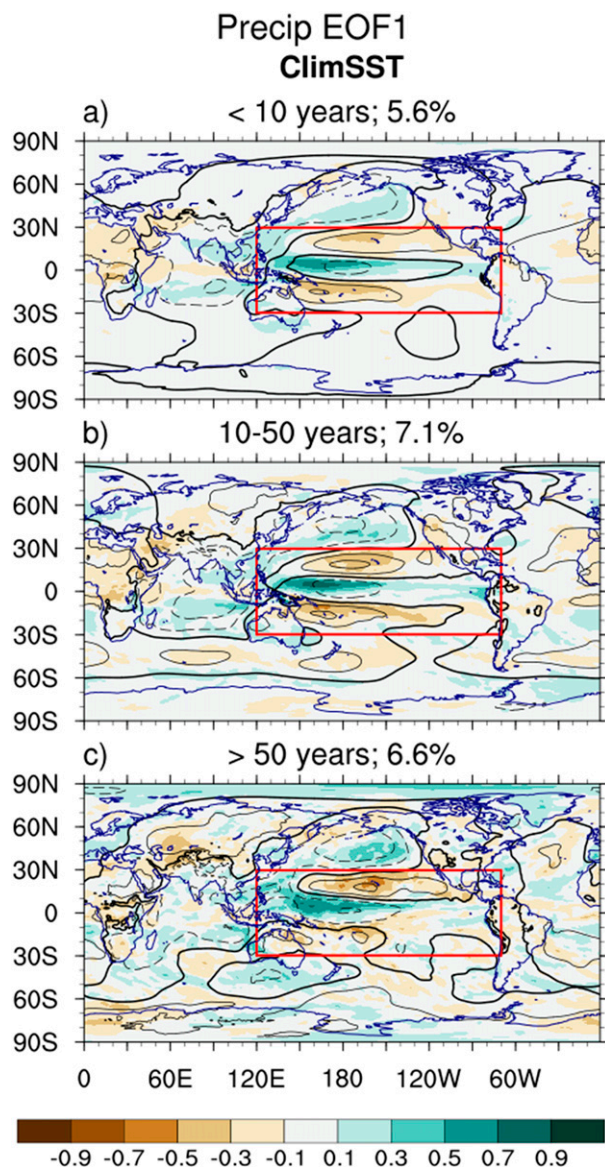


FIG. 12. As in Fig. 11, but for the ClimSST run.

and weakens in the case of the Coupled run. Moreover, in the Coupled run on the multidecadal time scale, the tropical Pacific linkage to the PSA is mainly confined to south of the equator (Fig. 13c), which differs from the ENSO-like pattern based directly on the tropical precipitation EOF (Fig. 11c). No such distinction is evident for the SlabOcean run at the multidecadal time scale, which exhibits nearly identical global-scale patterns whether based on the first EOF (EOF1) of South Pacific SLP (Fig. 13f) or tropical Pacific precipitation (Fig. 11f). If the analysis is based on the EOF of North Pacific SLP instead of the South Pacific, similar results are found: that is, the SlabOcean run also exhibits stronger teleconnections between the northern extratropics and the

tropical Pacific at the multidecadal time scale compared to the interannual time scale, while the Coupled run shows the opposite (Fig. S10 in the supplementary material). EOF analyses of tropical Pacific SST further show that multidecadal ENSO-like variability is stronger in the SlabOcean run than the Coupled run (Fig. S11 in the supplementary material). This indicates a possible negative role of ocean dynamics in the tropical–extratropical teleconnections and the development of ENSO-like variability at the multidecadal time scale.

4. Conclusions and discussion

We have studied tropical precipitation variability in fully coupled, slab ocean, and fixed-SST runs whose component models, when active, are identical. The main goal was to identify atmospheric and oceanic origins of tropical precipitation variability and to understand the thermodynamic and dynamic nature of the ocean-induced precipitation variability. We obtain the atmospheric component of precipitation variability from the fixed-SST run and the ocean-induced component from the difference between the fully coupled and fixed-SST runs. Note that this definition of ocean-induced precipitation variability does not differentiate between the impact of internal oceanic variability and that of ocean–atmosphere interaction. While internal oceanic variability has been shown to produce a multidecadal spectral peak in SST in the northern North Atlantic in association with fluctuations of the thermohaline circulation (Delworth and Zeng 2016; Delworth et al. 2017), we find no evidence for spectral peaks beyond that associated with the interannual ENSO phenomenon in either tropical precipitation (Fig. 2) or tropical SST (Fig. S3) in the fully coupled simulation. Thus, most of the ocean-induced tropical precipitation variability studied here likely originates from ocean–atmosphere interaction instead of internal oceanic variability. Further experiments are needed to provide conclusive results.

Our analyses of the fixed-SST simulation show that substantial precipitation variability is internally generated by the atmosphere. This atmospheric intrinsic precipitation variability exhibits a red spectrum at submonthly time scales and a white spectrum at longer time scales. The pattern of the atmospheric intrinsic precipitation variance is similar to the pattern of precipitation climatology at all time scales examined (submonthly–multidecadal). Because of the lack of substantial SST variability at submonthly time scales, the high-frequency precipitation variability is almost identical with and without oceanic influence. At lower frequencies, however, the ocean has a strong impact.

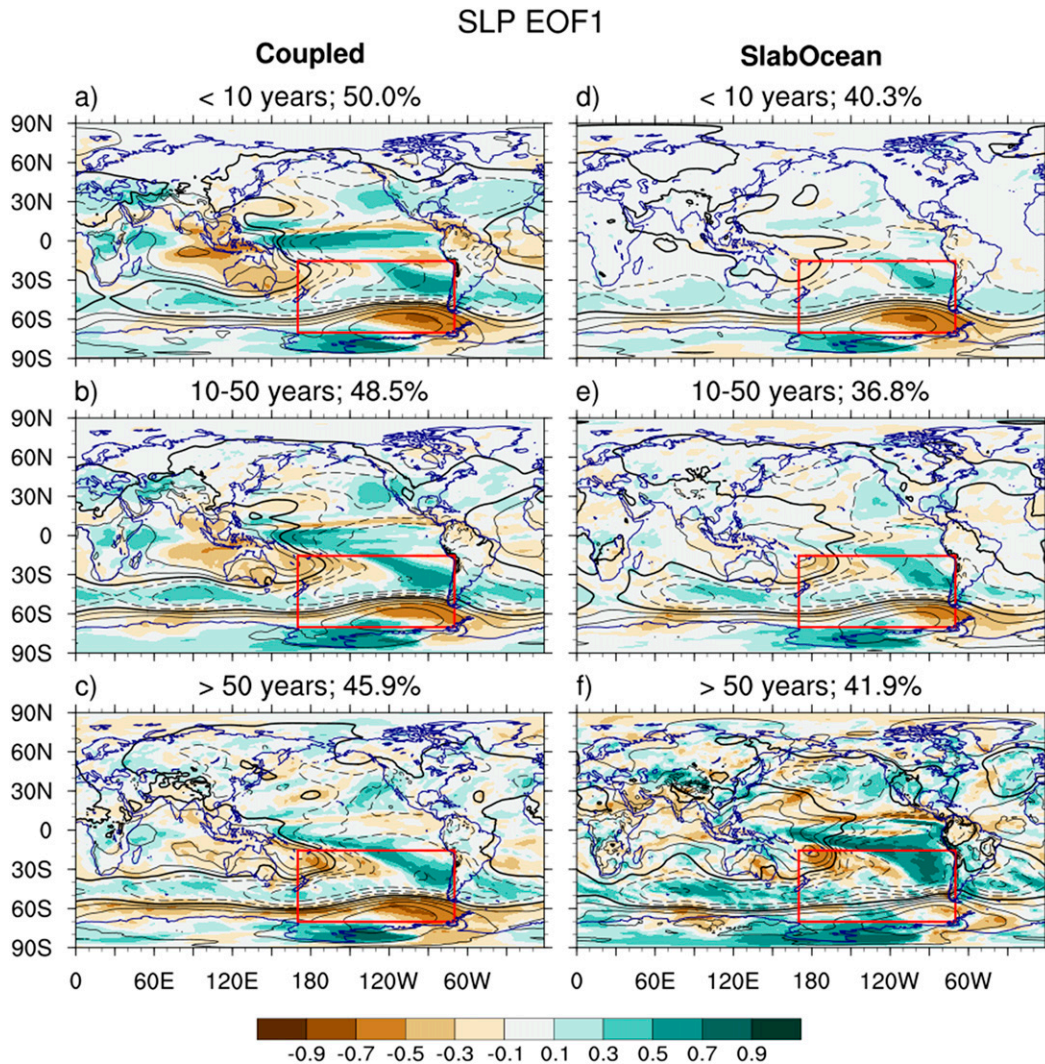


FIG. 13. Linear correlation of precipitation (shading) and SLP (contour) anomalies with the leading PC of SLP anomalies in the South Pacific region, which is marked by the red boxes. Data are the annual mean output filtered by (a),(d) 10-yr high pass, (b),(e) 10–50-yr bandpass, and (c),(f) 50-yr low pass. Results are from the (left) Coupled and (right) SlabOcean runs. Contour interval is 0.2. Dashed contours represent negative values. The zero contour is thickened. Variance explained by EOF1 is shown in the title of each panel.

At the interannual time scale and beyond, the role of ocean in generating precipitation variability varies with region. Ocean increases precipitation variability over most of the tropical oceans but reduces it over some parts of the subtropics preferentially in the summer hemisphere. In the equatorial Pacific and equatorial Indian Ocean, the ocean-induced precipitation is primarily driven by ocean dynamics. Over the rest of the tropical oceans, however, it is dominated by the thermodynamic coupling with the ocean mixed layer.

In addition to its impact on precipitation variability, ocean also affects the simulation of precipitation climatology. In particular, precipitation climatology along the equator of the Pacific is reduced by nearly half when

SST variability is not included. This has great implications for the future design of AMIP-type experiments, since it has been a common practice to neglect SST variability in simulations that only aim to study the time mean changes in precipitation (e.g., externally forced mean climate change). Our results showed that the inclusion of accurate SST variability is necessary for simulating the time mean precipitation in this key region.

The pattern of the ocean-induced precipitation variability is similar to the pattern of the pointwise precipitation–SST regression. In regions where the regression is positive, SST forcing dominates the precipitation–SST relationship and amplifies precipitation variability. In regions where the regression is negative, however, the SST

anomaly is largely a response to the negative precipitation feedback and subsequently acts to suppress precipitation variability. ENSO is also important for the establishment of the precipitation–SST relationship by enhancing the SST forcing at the equator and inducing a negative precipitation feedback in the off-equatorial regions. Interestingly, the negative precipitation–SST relationship generally occurs at the center of the ITCZ and in the summer hemisphere subtropics, where the sea surface is relatively warm. Observational studies showed that precipitation and cloud formation tend to keep SST below a certain maximum value (e.g., [Waliser and Graham 1993](#); [Sud et al. 1999](#)), and negative precipitation feedback is therefore likely stronger in regions of warm SST. However, future studies are needed to assess the simulation of such processes in climate models.

Assessing the simulation of the ocean-induced precipitation variability is a challenge partly because of the difficulty in separating the ocean-induced variance from the total variance in observations. However, the pattern similarity between the ocean-induced precipitation variance and the precipitation–SST regression allows us to assess the former through the latter. The coupled CESM simulates overall reasonable precipitation–SST regression; its biases are largely associated with biases in the position of the ITCZ.

Although we have focused mostly on the relationship between precipitation and SST anomalies, fluctuations in the SST gradient can also be important in generating precipitation variability. In particular, the observational study by [Li and Carbone \(2012\)](#) showed a greater role for the local SST gradient than the local SST in triggering individual rainfall events over the tropical western Pacific. On a seasonal mean basis, however, we found that precipitation variability is more closely related to the local SST rather than the local SST gradient in both observations and the fully coupled simulation (Figs. S6 and S7), except in the center of the northern ITCZ in DJF and directly along the equator in the western Pacific in both DJF and JJA. The issue of the relative importance of the local SST versus SST gradient on precipitation variability as a function of temporal scale merits additional investigation.

We briefly presented an EOF analysis to study the spatial characteristics of the precipitation variability simulated by the three CESM configurations. The leading modes of tropical Pacific precipitation show very different amplitude and spatial structures with and without ocean coupling. A similar ENSO-like precipitation pattern appears in the Coupled run at decadal and multidecadal time scales and in the SlabOcean run at all time scales longer than one year. In the Coupled run, the ENSO-like mode and its teleconnection with the extratropical circulation weaken as the time scale lengthens. In contrast, the SlabOcean run shows a stronger ENSO-like mode and a

more robust tropical–extratropical teleconnection at longer time scales. This suggests that the role of ocean dynamics in driving tropical Pacific variability likely diminishes with increasing time scale. Particularly at time scales longer than 50 years, the ENSO-like variability in the SlabOcean run becomes stronger than that in the Coupled run.

The stronger multidecadal variability in the SlabOcean run indicates a negative feedback between ocean circulation and SST variability at low frequencies, which was proposed by [Di Nezio \(2011\)](#). At the interannual time scale, ENSO is initialized by changes in the thermocline depth associated with the reflected Kelvin wave. The Kelvin wave is generated because wind-driven Rossby waves do not arrive at the western boundary in phase (e.g., [Cane and Sarachik 1981](#)). At longer time scales, however, the wind forcing and ocean adjustment are able to maintain a closer balance, resulting in a weaker Kelvin wave and weaker thermocline forcing. As a result, changes in the thermocline no longer drive the SST variability but are instead in opposite phase to SST, providing a negative feedback. Such a mechanism likely causes the Coupled run to have a weaker ENSO-like variability than the SlabOcean run at the multidecadal time scale.

Natural precipitation variability at multidecadal and longer time scales has historically received less attention than its higher-frequency counterpart, mainly because of the lack of long-term observations. However, quantifying and understanding such variability is crucial for the interpretation of climate change, both in the recent past and coming decades. Many studies show that climate changes during a 50-yr span can be dominated by natural variability at regional scales, especially in the extratropics in winter ([Deser et al. 2012b, 2014](#); [Kay et al. 2015](#); [Deser et al. 2016](#)). This makes the assessment of historical climate simulations difficult, since the chronologies of the simulated internal variability need not match each other or the observation. [Figures 14a and 14b](#) show that the intermodel spread of 50-yr trends (1955–2005) in tropical precipitation from historical simulations in the CMIP5 archive is substantially larger than the multimodel mean trend, which is typically interpreted as the radiatively forced component. The small amplitude of the multimodel mean trend is in part due to the cancellation among the trends from the individual models. However, the spread in trends across the 35 members of the CESM large ensemble ([Fig. 14d](#)) is also larger than that model's forced response (given by the ensemble mean: [Fig. 14c](#)). This suggests that internal variability is large enough to mask the forced response, at least in the CESM, with implications for interpreting the observed record. Furthermore, the spread in 50-yr trends due to internal variability ([Fig. 14d](#)) is only

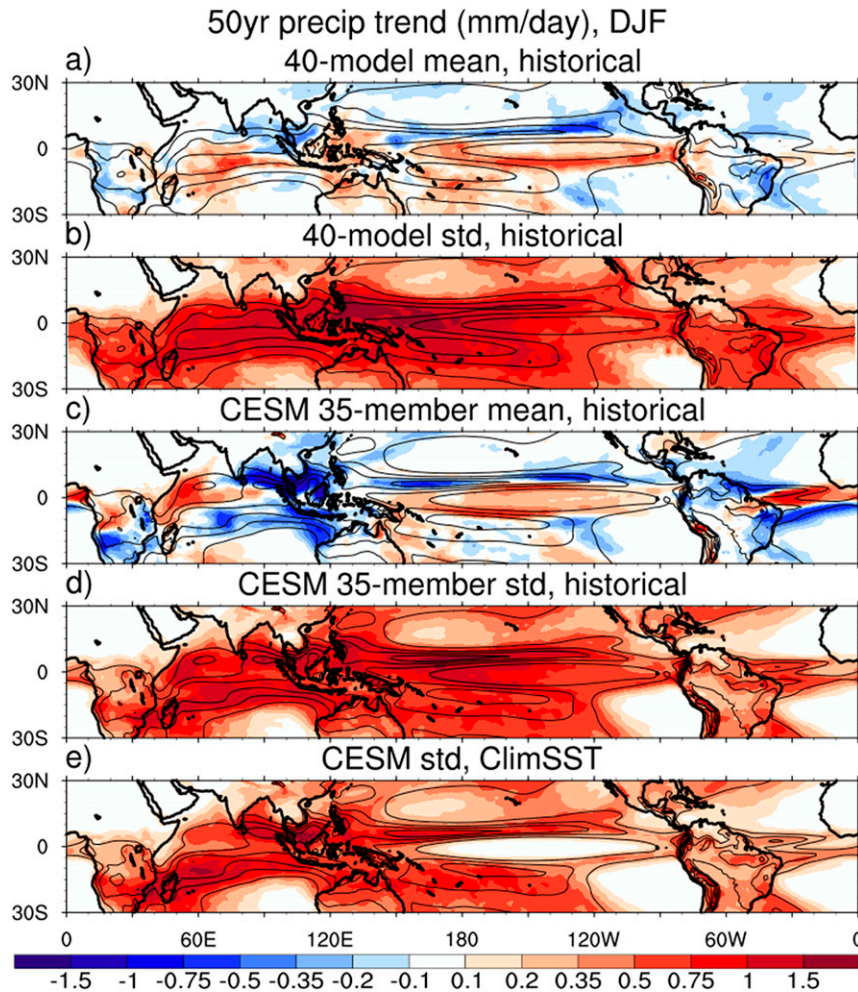


FIG. 14. The 50-yr DJF precipitation trend from the CMIP5 historical run and the CESM historical and preindustrial control runs. The historical trend is taken from the period of December 1955–November 2005. (a) The ensemble mean and (b) intermodel standard deviation of the historical precipitation trend from 40 CMIP5 models. (c) The ensemble mean and (d) intermember standard deviation of precipitation trend from the 35-member CESM historical runs, which only differ from each other slightly in their initial conditions. (e) The standard deviation of precipitation trends using nonoverlapping 50-yr segments from the ClimSST run. DJF precipitation climatology from the respective simulations is shown in contours, with an interval of 3 mm day^{-1} and starting at 3 mm day^{-1} . [The 40 CMIP5 models are BCC_CSM1.1, BCC_CSM1.1(m), BNU-ESM, CanESM2, CCSM4, CESM1(BGC), CESM1(CAM5), CESM1(FASTCHEM), CESM1(WACCM), CMCC-CESM, CMCC-CM, CMCC-CMS, CNRM-CM5, CNRM-CM5.2, EC-EARTH, FGOALS-g2, GFDL CM2.1, GFDL CM3, GFDL-ESM2G, GFDL-ESM2M, GISS-E2-H, GISS-E2-H-CC, GISS-E2-R, GISS-E2-R-CC, HadCM3, HadGEM2-CC, HadGEM2-ES, INM-CM4.0, IPSL-CM5A-LR, IPSL-CM5A-MR, IPSL-CM5B-LR, MIROC4h, MIROC5, MIROC-ESM, MIROC-ESM-CHEM, MPI-ESM-LR, MPI-ESM-MR, MPI-ESM-P, MRI-CGCM3, and MRI-ESM1. Expansions of acronyms are available online at <http://www.ametsoc.org/PubsAcronymList>.]

modestly less than the spread across the CMIP5 models (Fig. 14b), suggesting that internal climate variability, rather than the models' structural differences, is the main cause of spread.

Deser et al. (2012b) showed that the low-frequency precipitation variability in the extratropics is dominated

by atmospheric intrinsic dynamics. In the tropics, on the other hand, ocean is expected to have a much greater impact on precipitation. However, the spread in trends from nonoverlapping 50-yr segments of the ClimSST run is comparable to that from the 35-member CESM large ensemble (and that from the Coupled control run;

not shown), except at the equator (Fig. 14e). We have shown that the leading modes of large-scale tropical precipitation variability require interaction with the ocean. Therefore, the evolution of SSTs holds the key to future predictions of large-scale tropical precipitation. On regional scales, however, atmospheric intrinsic dynamics account for a substantial proportion of tropical precipitation variability, particularly over land regions, which may indicate limited predictability beyond the synoptic time scale.

Since all of our simulations were conducted with the CESM, future studies are encouraged to test the robustness of our results, particularly with higher-resolution models, which may more faithfully capture ENSO variability and its teleconnections (Jia et al. 2015) as well as submonthly variability.

Acknowledgments. We wish to thank Drs. Amy Clement, Ben Kirtman, and Pedro DiNezio for helpful discussions during the course of this work and Drs. Nathaniel Johnson and Liwei Jia for their internal review at GFDL. We appreciate the thoughtful comments and suggestions of the three anonymous reviewers. Thanks also go to Dr. Isla Simpson for providing the FullSST simulation and Dr. Todd Mitchell for calculating the pentad GPCP data. Jie He is supported by the Visiting Scientist Program at Princeton University.

REFERENCES

- Adler, R. F., and Coauthors, 2003: The Version-2 Global Precipitation Climatology Project (GPCP) monthly precipitation analysis (1979–present). *J. Hydrometeorol.*, **4**, 1147–1167, doi:10.1175/1525-7541(2003)004<1147:TVGPCP>2.0.CO;2.
- Back, L. E., and C. S. Bretherton, 2009: On the relationship between SST gradients, boundary layer winds, and convergence over the tropical oceans. *J. Climate*, **22**, 4182–4196, doi:10.1175/2009JCLI2392.1.
- Barsugli, J. J., and D. S. Battisti, 1998: The basic effects of atmosphere–ocean thermal coupling on midlatitude variability. *J. Atmos. Sci.*, **55**, 477–493, doi:10.1175/1520-0469(1998)055<0477:TBEOAO>2.0.CO;2.
- Bitz, C. M., K. M. Shell, P. R. Gent, D. A. Bailey, G. Danabasoglu, K. C. Armour, M. M. Holland, and J. T. Kiehl, 2012: Climate sensitivity of the Community Climate System Model, version 4. *J. Climate*, **25**, 3053–3070, doi:10.1175/JCLI-D-11-00290.1.
- Boyle, J. S., S. A. Klein, D. D. Lucas, H.-Y. Ma, J. Tannahill, and S. Xie, 2015: The parametric sensitivity of CAM5's MJO. *J. Geophys. Res. Atmos.*, **120**, 1424–1444, doi:10.1002/2014JD022507.
- Cane, M. A., and E. Sarachik, 1981: The response of a linear baroclinic equatorial ocean to periodic forcing. *J. Mar. Res.*, **39**, 651–693.
- Chiang, J. C. H., and B. R. Lintner, 2005: Mechanisms of remote tropical surface warming during El Niño. *J. Climate*, **18**, 4130–4149, doi:10.1175/JCLI3529.1.
- Clement, A., P. DiNezio, and C. Deser, 2011: Rethinking the ocean's role in the Southern Oscillation. *J. Climate*, **24**, 4056–4072, doi:10.1175/2011JCLI3973.1.
- , K. Bellomo, L. N. Murphy, M. A. Cane, T. Mauritsen, G. Rädcl, and B. Stevens, 2015: The Atlantic Multidecadal Oscillation without a role for ocean circulation. *Science*, **350**, 320–324, doi:10.1126/science.aab3980.
- , M. A. Cane, L. N. Murphy, K. Bellomo, T. Mauritsen, and B. Stevens, 2016: Response to comment on “The Atlantic Multidecadal Oscillation without a role for ocean circulation.” *Science*, **352**, 1527, doi:10.1126/science.aaf2575.
- Delworth, T. L., and F. Zeng, 2016: The impact of the North Atlantic Oscillation on climate through its influence on the Atlantic meridional overturning circulation. *J. Climate*, **29**, 941–962, doi:10.1175/JCLI-D-15-0396.1.
- , —, L. Zhang, R. Zhang, G. A. Vecchi, and X. Yang, 2017: The central role of ocean dynamics in connecting the North Atlantic Oscillation to the Atlantic multidecadal oscillation. *J. Climate*, doi:10.1175/JCLI-D-16-0358.1, in press.
- Deser, C., M. A. Alexander, and M. S. Timlin, 2003: Understanding the persistence of sea surface temperature anomalies in midlatitudes. *J. Climate*, **16**, 57–72, doi:10.1175/1520-0442(2003)016<0057:UTPOSS>2.0.CO;2.
- , and Coauthors, 2012a: ENSO and Pacific decadal variability in the Community Climate System Model version 4. *J. Climate*, **25**, 2622–2651, doi:10.1175/JCLI-D-11-00301.1.
- , A. Phillips, V. Bourdette, and H. Teng, 2012b: Uncertainty in climate change projections: The role of internal variability. *Climate Dyn.*, **38**, 527–546, doi:10.1007/s00382-010-0977-x.
- , —, M. A. Alexander, and B. V. Smoliak, 2014: Projecting North American climate over the next 50 years: Uncertainty due to internal variability. *J. Climate*, **27**, 2271–2296, doi:10.1175/JCLI-D-13-00451.1.
- , L. Terray, and A. S. Phillips, 2016: Forced and internal components of winter air temperature trends over North America during the past 50 years: Mechanisms and implications. *J. Climate*, **29**, 2237–2258, doi:10.1175/JCLI-D-15-0304.1.
- Di Lorenzo, E., G. Liguori, N. Schneider, J. C. Furtado, B. T. Anderson, and M. A. Alexander, 2015: ENSO and meridional modes: A null hypothesis for Pacific climate variability. *Geophys. Res. Lett.*, **42**, 9440–9448, doi:10.1002/2015GL066281.
- Di Nezio, P., 2011: Mechanisms of tropical Pacific climate change: Beyond the Bjerknes feedback. Ph.D. dissertation, Dept. of Meteorology and Physical Oceanography, University of Miami, 244 pp. [Available online at http://scholarlyrepository.miami.edu/oa_dissertations/567/.]
- Duchon, C. E., 1979: Lanczos filtering in one and two dimensions. *J. Appl. Meteor.*, **18**, 1016–1022, doi:10.1175/1520-0450(1979)018<1016:LFIOAT>2.0.CO;2.
- Frankignoul, C., 1985: Sea surface temperature anomalies, planetary waves, and air–sea feedback in the middle latitudes. *Rev. Geophys.*, **23**, 357–390, doi:10.1029/RG023i004p00357.
- , and K. Hasselmann, 1977: Stochastic climate models. Part II: Application to sea-surface temperature anomalies and thermocline variability. *Tellus*, **29A**, 289–305, doi:10.1111/j.2153-3490.1977.tb00740.x.
- Hansen, J., R. Ruedy, M. Sato, and K. Lo, 2010: Global surface temperature change. *Rev. Geophys.*, **48**, RG4004, doi:10.1029/2010RG000345.
- Hasselmann, K., 1976: Stochastic climate models. Part I: Theory. *Tellus*, **28A**, 473–485, doi:10.1111/j.2153-3490.1976.tb00696.x.
- He, J., and B. J. Soden, 2016: Does the lack of coupling in SST-forced atmosphere-only models limit their usefulness for climate change studies? *J. Climate*, **29**, 4317–4325, doi:10.1175/JCLI-D-14-00597.1.

- Huffman, G. J., R. F. Adler, D. T. Bolvin, and G. Gu, 2009: Improving the global precipitation record: GPCP Version 2.1. *Geophys. Res. Lett.*, **36**, L17808, doi:10.1029/2009GL040000.
- Hurrell, J. W., and Coauthors, 2013: The Community Earth System Model: A framework for collaborative research. *Bull. Amer. Meteor. Soc.*, **94**, 1339–1360, doi:10.1175/BAMS-D-12-00121.1.
- Jia, L., and Coauthors, 2015: Improved seasonal prediction of temperature and precipitation over land in a high-resolution GFDL climate model. *J. Climate*, **28**, 2044–2062, doi:10.1175/JCLI-D-14-00112.1.
- Jin, F.-F., 2001: Low-frequency modes of tropical ocean dynamics. *J. Climate*, **14**, 3874–3881, doi:10.1175/1520-0442(2001)014<3874:LFMOTO>2.0.CO;2.
- Kay, J. E., and Coauthors, 2015: The Community Earth System Model (CESM) Large Ensemble Project: A community resource for studying climate change in the presence of internal climate variability. *Bull. Amer. Meteor. Soc.*, **96**, 1333–1349, doi:10.1175/BAMS-D-13-00255.1.
- Klein, S. A., B. J. Soden, and N.-C. Lau, 1999: Remote sea surface temperature variations during ENSO: Evidence for a tropical atmospheric bridge. *J. Climate*, **12**, 917–932, doi:10.1175/1520-0442(1999)012<0917:RSSTVD>2.0.CO;2.
- Kwon, Y.-O., and C. Deser, 2007: North Pacific decadal variability in the Community Climate System Model version 2. *J. Climate*, **20**, 2416–2433, doi:10.1175/JCLI4103.1.
- Li, Y., and R. E. Carbone, 2012: Excitation of rainfall over the tropical western Pacific. *J. Atmos. Sci.*, **69**, 2983–2994, doi:10.1175/JAS-D-11-0245.1.
- Lindzen, R. S., and S. Nigam, 1987: On the role of sea surface temperature gradients in forcing low-level winds and convergence in the tropics. *J. Atmos. Sci.*, **44**, 2418–2436, doi:10.1175/1520-0469(1987)044<2418:OTROSS>2.0.CO;2.
- Lorenz, E. N., 1963: Deterministic nonperiodic flow. *J. Atmos. Sci.*, **20**, 130–141, doi:10.1175/1520-0469(1963)020<0130:DNF>2.0.CO;2.
- Luo, J.-J., and T. Yamagata, 2001: Long-term El Niño–Southern Oscillation (ENSO)-like variation with special emphasis on the South Pacific. *J. Geophys. Res.*, **106**, 22 211–22 227, doi:10.1029/2000JC000471.
- Newman, M., and Coauthors, 2016: The Pacific decadal oscillation, revisited. *J. Climate*, **29**, 4399–4427, doi:10.1175/JCLI-D-15-0508.1.
- Okumura, Y. M., 2013: Origins of tropical Pacific decadal variability: Role of stochastic atmospheric forcing from the South Pacific. *J. Climate*, **26**, 9791–9796, doi:10.1175/JCLI-D-13-00448.1.
- Pendergrass, A. G., and D. L. Hartmann, 2014: Two modes of change of the distribution of rain. *J. Climate*, **27**, 8357–8371, doi:10.1175/JCLI-D-14-00182.1.
- Pierce, D. W., T. P. Barnett, and M. Latif, 2000: Connections between the Pacific Ocean tropics and midlatitudes on decadal timescales. *J. Climate*, **13**, 1173–1194, doi:10.1175/1520-0442(2000)013<1173:CBTPOT>2.0.CO;2.
- Sardeshmukh, P. D., and B. J. Hoskins, 1988: The generation of global rotational flow by steady idealized tropical divergence. *J. Atmos. Sci.*, **45**, 1228–1251, doi:10.1175/1520-0469(1988)045<1228:TGOGRF>2.0.CO;2.
- Schneider, E. K., L. Bengtsson, and Z.-Z. Hu, 2003: Forcing of Northern Hemisphere climate trends. *J. Atmos. Sci.*, **60**, 1504–1521, doi:10.1175/1520-0469(2003)060<1504:FONHCT>2.0.CO;2.
- Schneider, N., and A. J. Miller, 2001: Predicting western North Pacific Ocean climate. *J. Climate*, **14**, 3997–4002, doi:10.1175/1520-0442(2001)014<3997:PWNPOC>2.0.CO;2.
- , and B. D. Cornuelle, 2005: The forcing of the Pacific decadal oscillation. *J. Climate*, **18**, 4355–4373, doi:10.1175/JCLI3527.1.
- Shinoda, T., M. A. Alexander, and H. H. Hendon, 2004: Remote response of the Indian Ocean to interannual SST variations in the tropical Pacific. *J. Climate*, **17**, 362–372, doi:10.1175/1520-0442(2004)017<0362:RRATIO>2.0.CO;2.
- Skinner, C. B., M. Ashfaq, and N. S. Diffenbaugh, 2012: Influence of twenty-first-century atmospheric and sea surface temperature forcing on West African climate. *J. Climate*, **25**, 527–542, doi:10.1175/2011JCLI4183.1.
- Sud, Y. C., G. K. Walker, and K.-M. Lau, 1999: Mechanisms regulating sea-surface temperatures and deep convection in the tropics. *Geophys. Res. Lett.*, **26**, 1019–1022, doi:10.1029/1999GL900197.
- Tang, Y., L. Li, W. Dong, and B. Wang, 2016: Tracing the source of ENSO simulation differences to the atmospheric component of two CGCMs. *Atmos. Sci. Lett.*, **17**, 155–161, doi:10.1002/asl.637.
- Trenberth, K. E., and D. J. Shea, 2005: Relationships between precipitation and surface temperature. *Geophys. Res. Lett.*, **32**, L14703, doi:10.1029/2005GL022760.
- Waliser, D. E., and N. E. Graham, 1993: Convective cloud systems and warm-pool sea surface temperatures: Coupled interactions and self-regulation. *J. Geophys. Res. Atmos.*, **98**, 12 881–12 893, doi:10.1029/93JD00872.
- Wang, B., Q. Ding, X. Fu, I.-S. Kang, K. Jin, J. Shukla, and F. Doblas-Reyes, 2005: Fundamental challenge in simulation and prediction of summer monsoon rainfall. *Geophys. Res. Lett.*, **32**, L15711, doi:10.1029/2005GL022734.
- Wu, R., B. P. Kirtman, and K. Pegion, 2006: Local air–sea relationship in observations and model simulations. *J. Climate*, **19**, 4914–4932, doi:10.1175/JCLI3904.1.
- Zhang, H., A. Clement, and P. Di Nezio, 2014: The South Pacific meridional mode: A mechanism for ENSO-like variability. *J. Climate*, **27**, 769–783, doi:10.1175/JCLI-D-13-00082.1.
- Zhang, R., 2008: Coherent surface-subsurface fingerprint of the Atlantic meridional overturning circulation. *Geophys. Res. Lett.*, **35**, L20705, doi:10.1029/2008GL035463.
- , R. Sutton, G. Danabasoglu, T. L. Delworth, W. M. Kim, J. Robson, and S. G. Yeager, 2016: Comment on “The Atlantic Multidecadal Oscillation without a role for ocean circulation.” *Science*, **352**, 1527, doi:10.1126/science.aaf1660.
- Zwiers, F. W., and H. von Storch, 1995: Taking serial correlation into account in tests of the mean. *J. Climate*, **8**, 336–351, doi:10.1175/1520-0442(1995)008<0336:TSCIAI>2.0.CO;2.